Carrier transport layer engineering of $Cs_2TiI_2Br_4$ halide double perovskite solar cell via SCAPS 1D: Approaching the Shockley-Queisser limit

Tasnim Tareq Ferdous [a], Sadia Sultana Urmi [a], Md Abdul Kaium Khan [b,*], Mohammad Abdul Alim [a]

[a] *Department of Electrical & Electronic Engineering, University of Chittagong, Chittagong, 4331, Bangladesh*
[b] *Department of Electrical Engineering, University at Buffalo, The State University of New York, Buffalo, NY, 14260, USA*

ARTICLE INFO

ABSTRACT

All-inorganic $Cs_2TiI_xBr_{(6-x)}$-based perovskite solar cells (PSCs) are recently attracting a lot of attention for their tunable bandgaps, earth abundance, non-toxicity, and ultra-stability. Among the $Cs_2TiI_xBr_{(6-x)}$ family of materials, $Cs_2TiI_2Br_4$ with a bandgap of ~1.38 eV has the potential to be an excellent single junction solar cell material with a theoretically higher Shockley-Queisser limit of power conversion efficiency (PCE). Its excellent optoelectronic properties make it a potential candidate for being the highest-performing PSC from the $Cs_2TiI_xBr_{(6-x)}$ family. In our study, a total of eight hole transport materials (P3HT, PTAA, Spiro-OMeTAD, PEDOT:Pss, CuSCN, CuI, NiO, and MoO_3) and six electron transport materials (PCBM, TiO_2, CdS, SnO_2, ZnO, and IGZO) were investigated to select suitable charge transport materials. The defect densities of interface and absorber, different absorber layer thicknesses, several metal work functions, series-shunt resistance, and temperature were investigated to derive the conditions for optimum performance. After thorough investigation, we derived four novel devices with the combination of all the organic and inorganic charge transport materials to provide optimum performance. Among them, the combination of inorganic SnO_2 and CuSCN as electron and hole transport layer respectively achieved the highest PCE of 23.41 %.

1. Introduction

Perovskite solar cells, which belong to the class of third-generation solar cell technologies that have undergone significant improvements, serve as a prominent example in the realm of renewable energy sources. These solar cells, named after the mineral perovskite, that exhibits a similar crystal structure, have gained considerable attention due to their potential to revolutionize the field of photovoltaics. By harnessing the unique properties of perovskite materials, these solar cells exhibit enhanced efficiency and performance compared to their predecessors, thereby paving the way towards a more sustainable future. The chemical structure of perovskites is a simple ABX_3 structure, where A denotes a cation, B denotes a metallic, and X denotes an oxygen or halide anion component [1,2]. For achieving simple and efficient production, as well as the ability to adapt to various fabrication techniques, the field of perovskite solar cells is expanding continuously. This is due to their exceptional optical and electrical properties, which include

* Corresponding author.
 E-mail address: mdabdulk@buffalo.edu (M.A.K. Khan).

the ability to fine-tune the bandgap, their remarkable capacity for absorbing light, their long carrier diffusion length, and their high level of tolerance towards defects. As a result of these significant advantages, PSCs have been attracting increasing attention within the scientific community and industry alike, leading to further exploration and development in this field. The efficiency of power conversion in single-junction solar cells based on PSCs has already surpassed 26 % [3,4]. The PSC's taking over the commercial photovoltaic industry is only a matter of time now.

Organic methylammonium (MA$^+$) and formamidinium (FA$^+$) have shown higher power conversion efficiency (PCE); however, these materials are hygroscopic, have less tolerance, and are in some cases unstable in ambient conditions. They are degradable at high temperatures, which indicates their volatility [5–8]. Another better-performing possible option is cesium-based all-inorganic perovskite. Cesium cation-based PSC devices exhibit better thermal stability than organic cation-based ones. In the case of the other materials in group I (K$^+$, Rb$^+$, and In$^+$) of the periodic table, the cations chemically forming PSCs are quite impossible because of their smaller atomic radius and other atomic characteristics [1,9,10]. In place of metallic B cations, Pb^{2+}-based PSCs have shown outstanding performance, but the toxicity and solubility of lead ions endanger the environment [11–15]. This concern is the main barrier to the widespread industrial manufacture of lead-halide perovskites, despite their performance. Sn^{2+}, Ge^{2+}, Bi^{3+}, Sb^{3+}, In$^+$, and Ag $^+$ are some alternate ions for toxic Pb^{2+} to obtain nontoxic all-inorganic PSCs [10,16–18]. Still, the majority of the lead-free PSC devices studied are not suitable for their chemical formation. Recently, halide perovskites containing Sn^{2+} cations have exhibited noteworthy outcomes. However, their susceptibility to moisture and oxygen in the surrounding environment, toxicity, and insufficient durability have been observed [12]. A new promising family can be Ti (IV)-based halide perovskite (HP), for they are earth-abundant, nontoxic, and stable. The HP family also possesses better optical properties as they have tunable defect properties and a bandgap ranging from 1.0 eV to 1.8 eV. In a study where Ju et al. [5] experimented on Cs$_2$TiI$_x$Br$_{(6-x)}$ (x = 0, 2, 4, and 6)-based double HPs using the melt-crystallization method, the material was tunable from 1.02 eV to 1.78 eV. Among this family, Cs$_2$TiBr$_6$ is the most studied material. Chen et al. [19] studied a PSC, where it was reported that the bandgap of this material is about 1.8 eV, keeping the absorber layer thickness at ~200 nm. The fabricated efficiency of the cell was 3.22 % and stable. From there, many computational studies were carried out, achieving higher efficiency using Cs$_2$TiBr$_6$ as the absorber layer and differing transport layers for charge carriers [20–28]. There are some limited experimental and numerical studies considering Cs$_2$TiI$_6$ as an absorber layer [29–32]. The reported bandgap of ~1.02 eV is low and is a potential candidate for the bottom cell in a tandem solar cell structure [32] rather than a single-junction perovskite solar cell [5].

The Shockley-Queisser limit suggests that a single junction PCE with a bandgap of ~1.3 eV can achieve the highest PCE, which is theoretically about 33 % of the total energy [33,34]. The tunability of the bandgaps in Cs$_2$TiI$_x$Br$_{(6-x)}$ can be achieved by altering the proportion of iodine and bromine halides. In a study, Ju et al. [5] observed that Cs$_2$TiI$_2$Br$_4$ (Cs$_2$TiI$_x$Br$_{(6-x)}$; x = 2) possesses a direct bandgap of ~1.38 eV and shows significant optical absorption. Yan et al. [35] reported that Cs$_2$TiI$_2$Br$_4$ has a longer carrier relaxation time (~2.2 ps for electron; ~0.7 ps for holes) than the studied materials, Cs$_2$TiBr$_6$ (~1.4 ps for electron; ~0.9 ps for holes) and Cs$_2$TiI$_6$ (~1.4 ps for electron; ~1.3 ps for holes) as a result, the extraction of more hot charge carriers will take place. Therefore, the notable vibration of Ti-X is reduced in Cs$_2$TiI$_2$Br$_4$ due to their halide mixing. In other words, the hot electrons situated in a vicinity within a 10 nm radius of the perovskite/electron transport layer (ETL) interface can be efficiently extracted when considering a relaxation time of 2.2 ps. Most significantly, it is of utmost importance to note that the HP material demonstrates a remarkably elevated level of intrinsic and environmental stability, surpassing that of the widely embraced Pb-containing HPs [36]. Nonetheless, it is imperative to acknowledge that there remains a notable lack in terms of the extensive array of experimental or simulated research endeavors that have been undertaken thus far utilizing this immensely promising halide-double perovskite material as an absorber layer and the lack of comprehensive study on Cs$_2$TiI$_2$Br$_4$-based PSCs calls for a thorough investigation into different facets of designing high-performing Cs$_2$TiI$_2$Br$_4$-based PSCs.

The primary objective of this study is to introduce a computational approach that incorporates a comprehensive analysis of various organic and inorganic carrier transport materials. To achieve this, we have meticulously considered the implementation of Spiro-OMeTAD, P3HT, PEDOT:Pss, and PTAA as the organic hole transport materials (HTLs) and CuSCN, CuI, NiO, and MoO$_3$ as inorganic HTLs. Also, PCBM, TiO$_2$, CdS, SnO$_2$, ZnO, and IGZO are chosen as electron transport materials (ETLs), whereas PCBM is the only organic ETL chosen for its superior carrier mobility than other organic ETL and being the most frequently used organic ETL. This extensive investigation allows us to gain valuable insights into the performance and efficiency of the proposed PSCs, unraveling the interactions between the transport charge carriers and the overall device architecture. Throughout this study, in-depth simulation was the key to selecting the best organic and inorganic charge transport layers, keeping our novel halide double Cs$_2$TiI$_2$Br$_4$ perovskite as the absorber layer. The material parameters for Cs$_2$TiI$_2$Br$_4$ are extracted from several Cs$_2$TiI$_x$Br$_{(6-x)}$ (x = 0, 2, 4, and 6)-based valid experimental studies. From the studied materials, we have identified the optimum organic/inorganic HTLs and organic/inorganic ETLs for Cs$_2$TiI$_2$Br$_4$ and their combination provided us with four possible devices. After optimization of interface defects, absorber defects, and absorber thickness, we propose an optimized perovskite solar cell with n-i-p type FTO/SnO$_2$/Cs$_2$TiI$_2$Br$_4$/CuSCN/Au structure with all-inorganic charge transport layers. Further, we investigated the back contact, series-shunt resistance, and temperature to find overall optimum conditions for the device. We believe this study will aid experimentalists to make a better choice of carrier transport layers and motivate them to fabricate this highly promising device.

2. Materials and methodology

2.1. Computation in SCAPS-1D

We utilized the SCAPS-1D simulator to simulate the photovoltaic (PV) properties of the photovoltaic solar cells (PSCs) currently

under examination, which was developed by Burgelman et al. [37]. The tool uses semiconductor physics principles, including Poisson's equation and the continuity equations for electrons and holes. These equations also involved drift and diffusion currents PAL [38–41].

$$\frac{d^2}{dx^2}\psi(x) = \frac{e}{\xi_0\xi_r}\left(\rho(x) - n(x) + N_D - N_A + \rho_p - \rho_n\right) \tag{1}$$

$N_{A/D}$ represents acceptor/donor concentration, and electrostatic potential is represented by ψ. e represents the charge of the electron and $\xi_{r/0}$ denotes relative/vacuum permittivity, respectively. The hole concentration and the electron concentration are represented by p and n. $\rho_{n/p}$ denotes the electron/hole distributions, respectively. The principles of continuity can be demonstrated as follows:

$$-\frac{\partial j_p}{\partial x} - U_p(n,p) + G = 0 \tag{2}$$

$$-\frac{\partial j_n}{\partial x} - U_n(n,p) + G = 0 \tag{3}$$

Here, the electron and hole current densities are represented by $j_{n/p}$, while G denotes the carrier generation rate.

$$J_n = qn\mu_n E + qD_n\frac{\partial n}{\partial x} \tag{4}$$

$$J_p = qn\mu_p E + qD_p\frac{\partial p}{\partial x} \tag{5}$$

The relationships between drift and diffusion currents, which are employed to derive the total current density in the presence of an electric field and concentration gradient. The $D_{n/p}$ mentioned in the above equations denote the electron and hole diffusion coefficients, respectively.

2.2. Cs₂TiI₂Br₄-based PSC structure

We initiated simulations using a standard n-i-p type perovskite solar cell configuration. This setup featured a front contact composed of fluorine-doped tin oxide (FTO), a Cs$_2$TiI$_2$Br$_4$ layer as the absorber, and various combinations of hole transport layers (HTLs) and electron transport layers (ETLs), culminating in a back contact made of gold (Au).

Table 1 and Table 2 provide all the material parameters used throughout the study while Table 1 provides data for HTLs, Table 2 provides data for ETLs and the perovskite absorber layer (PAL). For individual layers, the defect type is neutral with a gaussian distribution and the energy with respect to the reference is 0.6 eV above E$_v$ with a characteristic energy of 0.1 eV. The defect density of interfacial layer between charge transport layers (HTL/ETL) and PAL layer is set at 2.25×10^{12} cm^{-2} for the initial computation. Our simulations replicated exposure to AM 1.5G solar radiation, with a power density of 100 mW/cm^2 and a temperature of 300 K. We set the shunt resistance to 4200 Ω-cm^2 the series resistance to 1 Ω-cm^2.

3. Results and discussion

In this work, we have built our HTLs and ETLs from both organic and inorganic categories. In the rigorous selection procedure, we have selected best electron/hole transport layer among all section. We then combined these best performing charge transport materials into four novel devices. From all the combined categories of organic and inorganic transport layers, we have examined the

Table 1
Simulation parameters for organic and inorganic HTLs.

Parameters	P3HT	PEDOT:Pss	PTAA	Spiro-OMeTAD	CuSCN	CuI	MoO₃	NiO
d(nm)	50	50	50	50	50	50	50	50
E_g (eV)	2	2.2	2.95	2.88	3.6	3.1	3	3.8
χ (eV)	3.2	2.9	2.3	2.05	1.7	2.1	2.5	1.46
ε_r	3	3	3.5	3	10	6.5	12.5	10.7
N_c (cm⁻³)	1×10^{20}	2.2×10^{15}	2.5×10^{18}	2.2×10^{15}	2.2×10^{19}	2.8×10^{19}	2.2×10^{18}	2.8×10^{19}
N_v (cm⁻³)	1×10^{20}	1.8×10^{18}	1.8×10^{19}	1.8×10^{19}	1.8×10^{18}	1×10^{19}	1.8×10^{19}	1×10^{19}
μ_n (cm²/ V s)	1×10^{-4}	2×10^{-2}	1×10^{-4}	2×10^{-4}	1×10^{2}	1×10^{2}	25×10^{-1}	1.2×10^{1}
μ_p (cm²/ V s)	1×10^{-4}	2×10^{-4}	1×10^{-4}	2×10^{-4}	2.5×10^{1}	4.39×10^{1}	1×10^{2}	28×10^{-1}
N_D (cm⁻³)	–	–	–	–	0	0	0	0
N_A (cm⁻³)	1×10^{16}	3.17×10^{14}	1×10^{18}	2×10^{19}	1×10^{18}	1×10^{18}	1×10^{18}	1×10^{18}
N_t (cm⁻³)	1×10^{14}	1×10^{14}	1×10^{14}	1×10^{14}	1×10^{14}	1×10^{14}	1×10^{14}	1×10^{14}
$\sigma_{n/h}$ (cm²)	1×10^{-15}	1×10^{-15}	1×10^{-15}	1×10^{-15}	1×10^{-15}	1×10^{-15}	1×10^{-15}	1×10^{-15}
$V_{th(n/h)}$ (cm/s²)	1×10^{7}	1×10^{7}	1×10^{7}	1×10^{7}	1×10^{7}	1×10^{7}	1×10^{7}	1×10^{7}
Reference	[32]	[42,43]	[44]	[45]	[22]	[22]	[22]	[22]

Table 2

Simulation parameters for FTO, organic and inorganic ETLs, and PAL.

Parameters	FTO	TiO$_2$	CdS	SnO$_2$	ZnO	IGZO	PCBM	Cs$_2$TiI$_2$Br$_4$
d(nm)	150	50	50	50	50	50	50	200
E_g (eV)	3.5	3.2	2.4	3.5	3.3	3.05	2	1.38
χ (eV)	4.4	4.1	4.18	4	4.1	4.16	4.2	4.0
ε_r	9	9	10	9	9	10	3.9	4.35
N_c (cm^{-3})	2.2×10^{18}	1.0×10^{21}	2.2×10^{18}	2.2×10^{17}	2.2×10^{18}	5×10^{18}	2.5×10^{21}	5.65×10^{19}
N_v (cm^{-3})	1.8×10^{19}	2.0×10^{20}	1.9×10^{19}	2.2×10^{16}	1.9×10^{19}	5×10^{18}	2.5×10^{21}	2.00×10^{19}
μ_n (cm^2/Vs)	20	20	100	20	100	15	0.2	0.236
μ_p (cm^2/Vs)	10	10	25	10	25	0.1	0.2	0.171
N_D (cm^{-3})	1×10^{19}	1×10^{19}	1×10^{18}	1×10^{18}	1×10^{18}	1×10^{18}	2.93×10^{17}	3×10^{19}
N_A (cm^{-3})	0	0	0	0	0	0	0	3×10^{18}
N_t (cm^{-3})	–	1×10^{14}	1×10^{14}	1×10^{14}	1×10^{14}	1×10^{14}	1×10^{14}	4.16×10^{15}
$\sigma_{n/h}$ (cm^2)	–	2×10^{-14}	2×10^{-14}	2×10^{-14}	2×10^{-14}	2×10^{-14}	2×10^{-14}	1×10^{-15}
$V_{th(n/h)}$ (cm/s^2)	1×10^7	1×10^7	1×10^7	1×10^7	1×10^7	1×10^7	1×10^7	1×10^7
Reference	[32]	[32]	[22,32]	[22,32]	[22,32]	[46]	[42]	[5,27,32]

performance parameters at different interfacial and absorber defect densities and thicknesses of PAL layer to select the best possible device.

Furthermore, we have deduced the cell performance of the current density vs. voltage curve, quantum efficiency curve and compared all the four optimized device performance and other important factors thoroughly. Finally, we analyzed the behavior of the optimized PSC on different materials' work functions for optimized electrode selection, aka back-contact on the best performing device. We have also taken the effects of shunt-series resistance, and temperature into account for the computational study. Throughout this experiment, we come up with a novel device with higher efficiency and better performance.

3.1. Optimization of HTL

For the hole transport layer (HTL) optimization section, we are going to simulate and understand the device's performance by adding different organic and inorganic hole transport materials to the HTL layer. We will be considering parameters like the fill factor (FF), short circuit current (J$_{SC}$), open circuit voltage (V$_{OC}$), and power conversion efficiency (PCE) of the device. With the use of the energy band diagram of our halide double absorber, Fig. S1 (supplementary information) describes the valence band offset (VBO) of various organic and inorganic HTLs. For the total HTL layer optimization study, we have considered the basic structure of FTO/TiO$_2$/Cs$_2$TiI$_2$Br$_4$/HTLs/Au, where the CuSCN, MoO$_3$, CuI, and NiO as inorganic hole transport materials (HTLs) and Spiro-OMeTAD, PEDOT:Pss, P3HT, and PTAA as organic HTLs. The interfacial defect type we worked on was Gaussian-Neutral, where 2.25×10^{12} cm^{-2} were the calculated interface defect density. Table 1 contains all the simulation parameters in the SCAPS-1D tool for the mentioned organic and inorganic HTLs.

3.1.1. Organic HTL optimization

We utilized organic hole transport materials (HTLs), i.e., P3HT, PEDOT:Pss, PTAA, and Spiro-OMeTAD for the simulation. Organic HTLs have been widely used for perovskite layer fabrication since the very beginning of the perovskite research domain. Spiro-OMeTAD is the most widely used hole transport material of all. Fig. 1 (a) shows the current density vs. voltage (J-V) characteristics of the organic HTLs. From Fig. 1 (b), The power conversion efficiency (PCE) is about 5.79 % for Spiro-OMeTAD, whereas the PCE deteriorates to 5.51 %, 5.17 %, and 3.27 % for PTAA, PEDOT:Pss, and P3HT, respectively. As we also see from Table S1 (supplementary information), the V$_{OC}$, FF, and J$_{SC}$ are also decreasing gradually in accordance with the above-mentioned hierarchy. From, the J-V
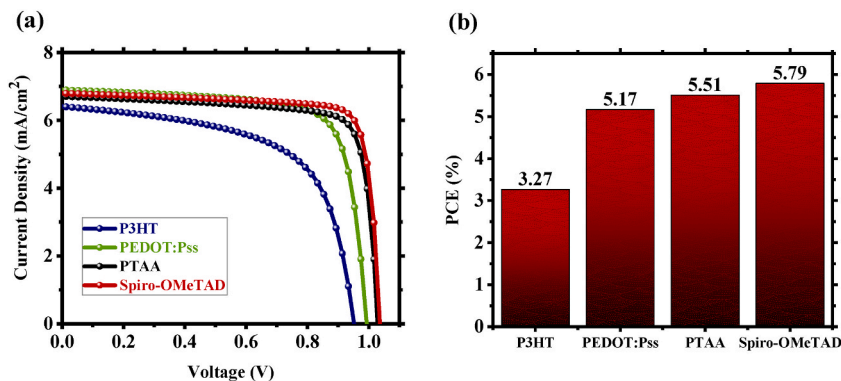

Fig. 1. Comparison of (a) J-V characteristics; (b) PCE for different organic HTLs.

characteristics curve of the organic hole transport materials depicted in Fig. 1(a), we can closely see that besides P3HT, all the other materials have shown closer open circuit current density and the highest open circuit voltage of 1.04 V (Table S1) is achieved in the case of Spiro-OMeTAD. The band diagrams of Spiro-OMeTAD, PEDOT:Pss, P3HT, and PTAA are shown in Fig. S1 (supplementary information), where Spiro-OMeTAD possesses the lowest valence band offset (VBO) of −0.08 eV among all the organic HTLs leading to its dominant performance. As a result, we chose Spiro-OMeTAD as the best possible organic HTL for $Cs_2TiI_2Br_4$-based PSCs.

3.1.2. Inorganic HTL optimization

Here, our main goal is to select the highest-performing inorganic hole transport material for $Cs_2TiI_2Br_4$-based PSCs. For this purpose, we have taken several inorganic hole transport materials such as CuO_2, CuSCN, CuI, NiO, and MoO_3. The simulated J-V characteristics are shown in Fig. 2(a). We compared the J-V characteristics of CuSCN, CuI, NiO, and MoO_3 as inorganic HTLs, evaluated of all the corresponding substances, open circuit voltage (V_{OC}), short circuit current (J_{SC}), fill factor (FF), and power conversion efficiency (PCE). All the inorganic HTLs show promising performance, and in terms of stability factors, these materials exceed the organic ones [53]. Fig. S1 (supplementary information) shows the respective energy band diagram of the inorganic HTLs with CuSCN possessing the lowest valence band offset (VBO) of −0.08 eV among all the inorganic HTLs and together with its excellent hole mobility, it produces comparatively better performance. From Fig. 2(b), the efficiency of our device is 6.06 %, 5.81 %, 5.97 %, and 5.99 % for CuSCN, CuI, NiO, and MoO_3, respectively. From Table S1 (supplementary information), we can closely observe the overall performance of all the four inorganic HTLs. As from Fig. S1 (supplementary information), other than MoO_3, the VBO is negative for all the remaining inorganic HTLs. As we know, a lower VBO means smaller barrier to flow the photo generated hole toward the back electrode, the least VBO for CuSCN and CuI corresponds to a very close J_{SC} of 7.17 mA/cm², 7.13 mA/cm² respectively. In the case of MoO_3 and NiO and the VBO is of accordingly +0.18 eV and - 0.18 eV respectively. Thus, we can evaluate from Table S1 (supplementary information) that they possess similar performance characteristics.

Considering all the HTLs, CuSCN demonstrates relatively better performance. There are some additional factors we are looking closely, i.e., CuSCN has a wider bandgap and better long-term ambient moisture stability [53–56]; it also has high optical transparency in comparison to the other inorganic HTLs. All in all, we choose CuSCN as the potential inorganic HTL for $Cs_2TiI_2Br_4$-based PSCs.

3.2. Optimization of ETL

Selection of ETL determines the electron conduction of the PSC device. Some important criteria like proper bandgap, electron mobility, generation and recombination rate are needed to gain better performance. We have taken the structure of FTO/ETL/$Cs_2TiI_2Br_4$/CuSCN/Au, where organic and inorganic electron transport materials such as PCBM, TiO_2, CdS, SnO_2, ZnO, and IGZO are chosen for the ETL optimization study. In the case of organic electron transport material, we have solely considered PCBM for its better electron mobility and other electrical properties. Available few other organic electron transport materials (ETLs) show very poor mobility and large conduction band offset (CBO), which are not suitable for computational study for our $Cs_2TiI_2Br_4$ based PSC. From Table S2 (supplementary information), we can see that organic PCBM shows an open circuit voltage; V_{OC} of 1.036 V, J_{SC} of 5.72 mA/cm², FF of 83.99 %, and PCE of around 4.98 %. Apart from PCBM, the other mentioned materials are optimum candidate for inorganic electron transport material optimization. These materials are mostly used for their easy fabrication and chemical characteristics. Important to note, the interface defect density throughout this study is the 2.25×10^{12} cm⁻². Table 2 shows the input simulation parameters for all the ETLs. For the simulation, $Cs_2TiI_2Br_4$ and CuSCN are used as the absorber and HTL, respectively. The energy band diagrams of the ETLs are shown in Fig. S2 (supplementary information). Fig. 3(a) illustrates the J-V characteristics of the ETLs. Fig. 3 (b) depicts the efficiency comparison. From all the performance comparisons we observe from Table S2 (supplementary information), SnO_2 is the best performing inorganic ETL of all. From Fig. S2 (supplementary information), CBO values of the ETLs are: 0.18 eV (CdS), 0 eV (SnO_2), 0.1 eV (TiO_2, ZnO), 0.16 eV (IGZO), and 0.2 eV (PCBM). The closer the band aligned with the $Cs_2TiI_2Br_4$, the better the extraction of electron and thus better performance. The allover performance parameters V_{OC}, J_{SC}, FF, and PCE for SnO_2 are 1.05 V, 9.41 mA/cm², 85.12 %, and 8.42 %, respectively.
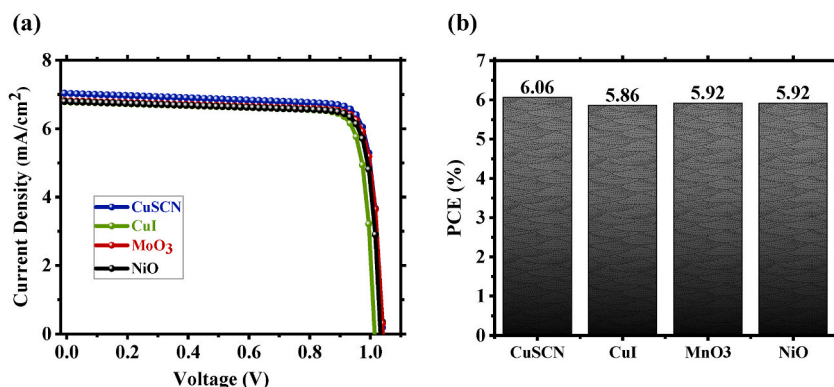

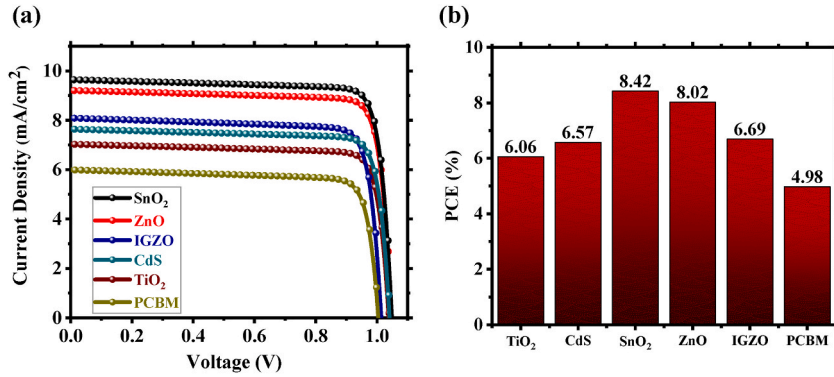**Fig. 2.** Comparison of (a) J-V characteristics curve; (b) PCE for different inorganic HTLs.

Fig. 3. Comparison of (a) J-V characteristics curve; (b) PCE for different ETLs.

SnO_2 has high electron mobility and better band alignment with the perovskite absorber layer, which is good for electron extraction. In recent ETL studies, SnO_2 is gaining attention as the most promising alternative to the commercially available TiO_2. TiO_2 is unstable to UV light, even in inert environments and with oxygen [47]. UV light exposure leads to rapid decay in device performance [48]. Changes to the charge transport layer can reduce device performance [47]. In order to prevent the TiO_2 layer from being photo-excited and to ensure that no photocurrent is lost from the device, Bella et al. [49] showed how to use a down-converting fluoropolymer that can pass the incoming UV light onto the perovskite layer as visible light. Thus, there are new scopes and vast opportunities for SnO_2 commercialization, which has recently been getting immense attention. Considering all these possibilities and performances, we have selected SnO_2 in the category of inorganic electron transport materials.

3.3. Defect density optimization

In recent years, the field of research concerning perovskite solar cells (PSCs) has made remarkable advancements, resulting in increased efficiency and the potential for cost-effective production. In order to improve the performance of photovoltaic solar cells (PSCs), it is imperative to investigate the impact of different variables on the functionality of the devices. The defect density is an important factor for PSC performance. Defects in the absorber layer decrease carrier lifetime and device efficiency. Therefore, reducing defect density is crucial for high efficiency. In this research, we have explored combination of both the inorganic and organic CTLs from the list of selected of HTLs and ETLs. The relationship between $Cs_2TiI_2Br_4$ defect density, interfacial defect density, and its thickness on PSC performance, of both devices were observed and optimized. Here, the device consisting of $FTO/SnO_2/Cs_2TiI_2Br_4/CuSCN/Au$ is mentioned as all-inorganic and the device that is constructed with the potential organic HTL: Spiro-OMeTAD and organic ETL: PCBM, which is constructed as $FTO/Spiro-OMeTAD/Cs_2TiI_2Br_4/PCBM/Au$ is mentioned as all-organic device throughout this study. The other two devices constructed from the combination of organic and inorganic HTL/ETL are described in *Section 2 of the supplementary information*. In this section we closely observe the performance and differences between both devices.

3.3.1. Optimization of interface defect density
The study of the defect density of the interfaces between the carrier transport layers (CTL)/perovskite absorber layer (PAL) for $FTO/SnO_2/Cs_2TiI_2Br_4/CuSCN/Au$, is conducted for a range of values spanning from 10^{12} cm^{-2} to 10^{16} cm^{-2}. To visually depict this analysis, Fig. 4 (a) is presented, showcasing the J-V characteristics for various defect densities at the interfaces. For this simulation, we
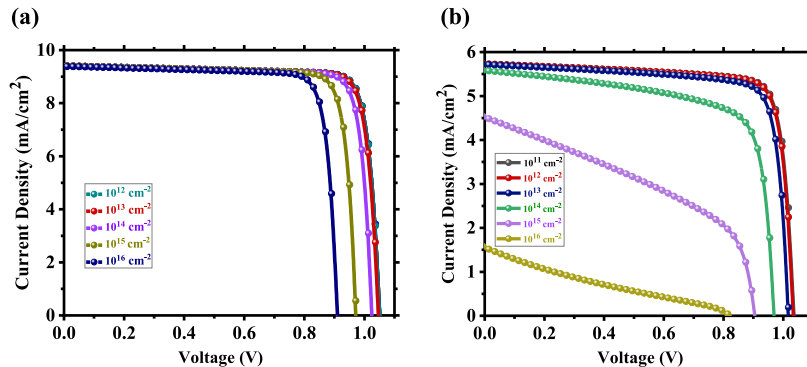

Fig. 4. J-V comparison of (a) all-inorganic CTL; (b) all-organic CTL for different interface defects.

have kept the perovskite's defect density and absorber thickness as mentioned in Table 2. Upon careful observation, it becomes apparent that for interfacial defect densities lower than 10^{13} cm^{-2}, the parameters exhibit minimal variation and the short-circuit current (J_{SC}) saturates. Conversely, as the interface defect density increases from 10^{10} cm^{-2} to 10^{14} cm^{-2}, the J_{SC} experiences a slight decrease from 9.4052 mA/cm^2 to 9.4050 mA/cm^2. However, it is important to note that the open-circuit voltage (V_{OC}) experiences a significant decrease as the defect density at the interface increases from 10^{10} cm^{-2} to 10^{14} cm^{-2}, resulting in a deterioration from 1.052 V to 1.031 V. This decline in V_{OC} can be attributed to the fact that interface defects introduce a greater number of traps at the recombination centers, ultimately leading to a reduction in overall performance. Therefore, we select the optimized interface defect to be 10^{12} cm^{-2} at which V_{OC} is 1.05 V, J_{SC} is 9.46 mA/cm^2, FF is 85.14 %, and PCE is 8.48 %. This optimized interfacial defect density is maintained in the next section of optimization.

As for the study conducted for FTO/Spiro-OMeTAD/Cs$_2$TiI$_2$Br$_4$/PCBM/Au, the all-organic CTL device, we can see a different behavior displayed in the J-V characteristics curve of Fig. 4 (b). Important to note there is no change in the value of absorber defect density and thickness, we have only varied interfacial defects between PAL/CTL from 10^{11} cm^{-2} to 10^{16} cm^{-2}. The J-V curve stays the same while the interfacial defect remains 10^{11} cm^{-2} or lower. The performance starts to slightly deteriorate at 10^{13} cm^{-2} and drastically going to the downfall, the higher the interfacial defects get. So, for all-organic CTL device, we have selected our device interfacial defect density to 10^{12} cm^{-2}, with achieving the performance a PCE of 4.89 %, V_{OC} of 1.035 V, J_{SC} of 5.76 mA/cm^2, and FF of 81.95 %.

3.3.2. Optimization of absorber defect density

To conduct an analysis on the impact of defect density, we have deliberately manipulated the defect density within a range of 10^{13} cm^{-3} to 2.5×10^{15} cm^{-3} of the PAL for FTO/SnO$_2$/Cs$_2$TiI$_2$Br$_4$/CuSCN/Au, all-inorganic CTL device. In order to visually represent our findings, Fig. 5 (a) has been included, which showcases the distinct J-V curves observed at various defect densities. Additionally, Fig. 5 (a) serves as an illustrative tool to elucidate the fact that when the defect density exceeds 10^{14} cm^{-3}, the short-circuit current density (J_{SC}) of the photovoltaic solar cell (PSC) experiences a notable degradation, plummeting from 21.05 mA/cm^2 for 10^{14} cm^{-3} to 16.51 mA/cm^2 for 10^{15} cm^{-3}. Conversely, when the defect density falls below 10^{14} cm^{-3}, it remains largely unaffected and stabilizes at a value of 10^{13} cm^{-3}. The underlying cause behind this deteriorative phenomenon lies in the amplification of the recombination rate, which exhibits an upward trend with the escalation of defect density. In the case of defect density at 1×10^{13} cm^{-3}, which is close to defect 10^{14} cm^{-3} shows the similar J-V characteristics. Thus, keeping the practical feasibility in mind, we selected an optimized defect density of 10^{14} cm^{-3} with a V_{OC} of 1.14 V, a J_{SC} of 21.05 mA/cm^2, an FF of 86.36 %, and a PCE of 20.80 %.

Whereas Fig. 5 (b) illustrates the observation of device FTO/PCBM/Cs$_2$TiI$_2$Br$_4$/Spiro-OMeTAD/Au while changing the PAL defect density from 10^{10} cm^{-3} to 10^{15} cm^{-3}. Important to note that the interfacial defect density and the PAL thickness of the device are maintained to 10^{12} cm^{-2} and 200 nm while optimizing both devices from Fig. 5. Best performance PCE of 6.82 % is achieved at 10^{13} cm^{-3} FTO/PCBM/Cs$_2$TiI$_2$Br$_4$/Spiro-OMeTAD/Au all-organic CTL device. Both studies show a similar trend, i.e., in case of interface defect density optimization, both devices show an independence of current density for a particular range of variables as the higher the interfacial recombination rate, the greater the interface defect density thus reduction in V_{OC}. However, a contrasting case is observed in Fig. 5 (b), where open circuit voltage remains constant within a range of PAL defect densities for the all-organic CTL device, which is noteworthy.

3.4. Absorber thickness optimization

The thickness of the light-absorbing layer is a crucial aspect that needs to be carefully considered to optimize the overall efficiency of the PSC. The absorber layer's thickness determines the device's efficiency. The optimal thickness depends on the material's bandgap and absorption coefficient, which affect the device's ability to capture light. Thicker absorber layers can increase photon absorption but also increase recombination rates, reducing efficiency. Thinner absorber layers may reduce photon absorption but lower recombination rates, improving efficiency.
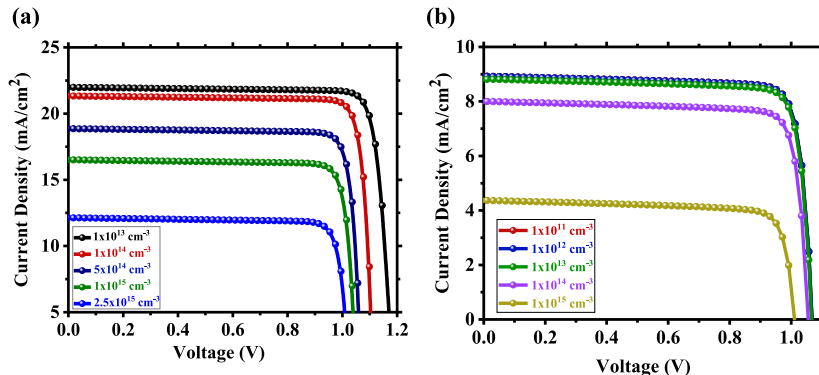

Fig. 5. J-V comparison of (a) all-inorganic CTL; (b) all-organic CTL for different absorber defects.

Fig. 6 represents our device's (all-inorganic CTL and all-organic CTL) performance varying PAL thickness from 100 nm to 800 nm. From Fig. 6, we can observe that with increasing thickness, the light-absorbing capacity of the cell increases drastically as the generation of charge carriers increases. Around 400 nm absorber thickness, the best performance is achieved for FTO/SnO$_2$/Cs$_2$TiI$_2$Br$_4$/CuSCN/Au all-inorganic CTL. In the case of all-organic CTL device, best performance is achieved around 300 nm. There is a tradeoff that we need to keep in mind: if the absorber thickness increases and exceeds the diffusion length, the recombination rate increases, and thus fewer charge carriers are collected from the charge transport layers. Here, the performance of the cell falls when absorber layer thickness is beyond 600 nm for both the devices. Thus, the optimal Cs$_2$TiI$_2$Br$_4$ absorber layer thickness is ~400 nm and ~300 nm for FTO/SnO$_2$/Cs$_2$TiI$_2$Br$_4$/CuSCN/Au and FTO/PCBM/Cs$_2$TiI$_2$Br$_4$/Spiro-OMeTAD/Au, accordingly. For the all-inorganic CTL device, the performance of the device at 400 nm shows a PCE of 23.41 % a V$_{OC}$ of 1.14 V, a J$_{SC}$ of 23.90 mA/cm^2, and an FF of 86.20 %. For the all-organic CTL structure, a PCE of 7.40 %, a V$_{OC}$ of 1.07 V, a J$_{SC}$ of 8.21 mA/cm^2 and an FF of 84.24 % is achieved.

3.5. Proposed device

Section 2 of the *supplementary information* shows the detailed optimization of the remaining two devices containing combinations of organic-inorganic CTLs. The two devices namely FTO/SnO$_2$/Cs$_2$TiI$_2$Br$_4$/Spiro-OMeTAD/Au and FTO/PCBM/Cs$_2$TiI$_2$Br$_4$/CuSCN/Au show comparable performance to the all-inorganic CTL and all-organic CTL devices optimized in the manuscript. All the crucial parameters are taken into account for enhancing the performance of our proposed device. We report a study on the effectiveness of a perovskite solar cell. This study's goal is to assess the efficiency of the optimization methods employed and establish the degree to which they have enhanced the device's performance. Fig. 7 illustrates the optimized J-V comparison curve and quantum efficiency (QE) curve of all the four devices. Table S3 (supplementary information) provides clear insight into the importance of the optimization parameters with a performance comparison between the initial state and optimized state of these 4 devices. From Fig. 7 we can see that the best performing optimized device with a PCE of 23.41 % and QE of around 82 % is achieved for all-inorganic CTL-based structure: FTO/SnO$_2$/Cs$_2$TiI$_2$Br$_4$/CuSCN/Au.

The all-organic CTL-based structure: FTO/PCBM/Cs$_2$TiI$_2$Br$_4$/Spiro-OMeTAD/Au shows a PCE of 7.40 % and QE of ~30 % within the visible spectrum. It's obvious from Fig. 7 that the choice of ETL is a crucial factor for the overall performance of Cs$_2$TiI$_2$Br$_4$-based PSCs with inorganic SnO$_2$ providing significant enhancement into device performance compared to the use of organic PCBM as ETL. For both SnO$_2$ and PCBM-based structures, variation in HTL provided minimal variation in device performance with almost overlapping performance curves. As a result, the top two PCE were achieved for SnO$_2$ based devices, where the use of inorganic CuSCN as HTL achieved 23.41 % efficiency compared to the 22.84 % efficiency of organic Spiro-OMeTAD as HTL. Therefore, both Spiro-OMeTAD and CuSCN can be considered as ideal HTL for Cs$_2$TiI$_2$Br$_4$-based PSCs. However, chlorobenzene can dissolve Cs$_2$TiI$_x$Br$_{(6-x)}$ rendering Spiro-OMeTADas an incompatible hole transport layer in practice [50]. Therefore, CuSCN can be thought of as the material of choice as HTL of Cs$_2$TiI$_2$Br$_4$-based PSCs for practical implementation.

Finally, we have attained our optimum device with inorganic SnO$_2$ and inorganic CuSCN as the ETL and HTL of the device and a total picture of the device and its corresponding energy levels can be found in Fig. 8. Table 3 exhibits the performance parameter comparison with existing works on the Cs$_2$TiI$_x$Br$_{(6-x)}$ family. As can be seen from the table, we have achieved competitive device performance with practically feasible device parameters, materials of choice and their corresponding thickness profile.

The best of the performance shown by the device, FTO/SnO$_2$/Cs$_2$TiI$_2$Br$_4$/CuSCN/Au among the rest three modeled devices, the energy band diagram study is added to understand the alignment of the energy bands, i.e. the band-offsets and its impact on noteworthy performance. Fig. 9 illustrates the band structures generated by SCAPS-1D. It is visible that the type of band offset at heterostructure is a staggered gap and its negative CBO forms a cliff-like confrontation at the junction from graphically illustrated in Fig. 8 (b). The energy cliff between ETL/PAL does not obstacle the mobility of photo-generated electrons, while the spike-like confrontation does the opposite work.
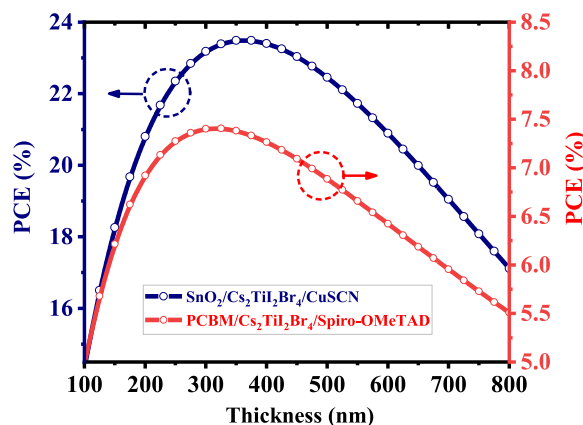

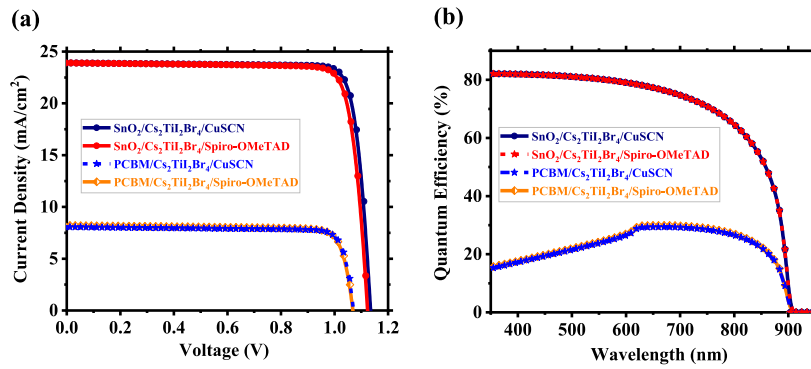**Fig. 6.** Power conversion efficiency as a function of absorber layer thickness.

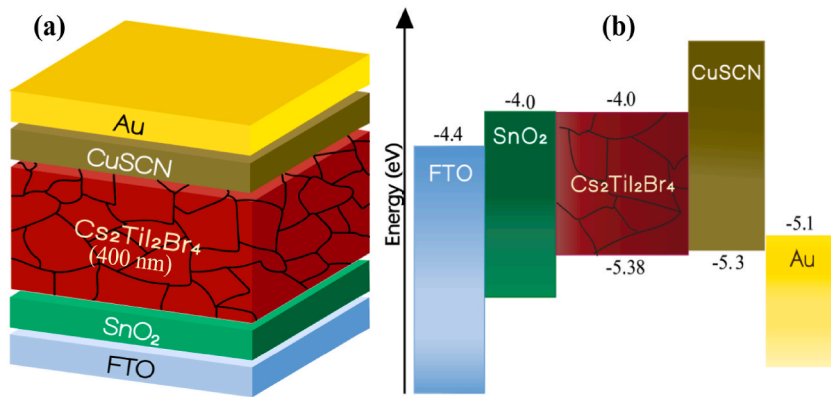**Fig. 7.** (a) J-V; (b) QE comparison of optimized PSCs.

Fig. 8. (a) Device structure; (b) energy band diagram of our proposed device: FTO/SnO$_2$/Cs$_2$TiI$_2$Br$_4$/CuSCN/Au.

Table 3
Comparison of the Cs$_2$TiI$_x$Br$_{6-x}$ family of PSCs with some existing numerical reports.

| Cell Structure	Absorber defect density (cm^{-3})	Absorber thickness (nm)	PCE (%)	J$_{SC}$ (mA/cm^2)	V$_{OC}$ (V)	FF (%)
CuSCN/Cs$_2$TiBr$_6$/CdS/Si [20]	–	1000	6.68	8.9	–	–
FTO/TiO$_2$/Cs$_2$TiBr$_6$/NiO/Au [21]	–	300	8.51	10.25	1.12	73.59
FTO/SnO$_2$/Cs$_2$TiBr$_6$/MoO$_3$/Au [22]	10^{14}	130	11.49	8.66	1.53	86.45
FTO/TiO$_2$/Cs$_2$TiBr$_6$/Cu$_2$O/Au [23]	10^{15}	800	14.68	25.82	1.10	51.74
ITO/NPB/Cs$_2$TiBr$_6$/PCBM/BCP/Ag [24]	10^{17}	350	16.85	16.66	1.29	78.10
AZO/TiO$_2$/Cs$_2$TiBr$_6$/PEDOT:PSS/Au [25]	–	200	17.83	18.20	1.38	71.00
CeO$_x$/Cs$_2$TiBr$_6$/NPB [26]	10^{15}	200	17.94	15.37	1.33	87.00
FTO/ZnO/Cs$_2$TiBr$_6$/MoO$_3$/Au [27]	10^{14}	400	18.15	13.60	1.53	87.23
FTO/BaSnO$_3$/Cs$_2$TiBr$_6$/CuSbS$_2$/Au [28]	10^{13}	1000	29.13	29.60	1.11	88.58
CuSCN/Cs$_2$TiI$_6$/CdS/Si [20]	–	1500	3.13	4.6	–	–
ITO/TiO$_2$/Cs$_2$TiI$_6$/CdTe/Au [29]	–	7830	15.06	25.08	1.39	43.17
FTO/TiO$_2$/Cs$_2$TiI$_6$/CuSCN/Ag [30]	10^{10}	1000	16.31	22.74	1.74	41
FTO/PEDOT: PSS/Cs$_2$TiI$_6$/C$_{60}$/Ag [31]	10^{10}	50	22.70	39.5	0.685	83.7
FTO/TiO$_2$/Cs$_2$TiI$_6$/CuI/Au [32]	10^{14}	300	21.17	32.93	0.79	81.42
FTO/SnO$_2$/Cs$_2$TiI$_2$Br$_4$/CuSCN/Au *	**10^{14}**	**400**	**23.41**	**23.90**	**1.14**	**86.20**
FTO/SnO$_2$/Cs$_2$TiI$_2$Br$_4$/Spiro-OMeTAD/Au *	**10^{14}**	**400**	**22.84**	**23.90**	**1.13**	**84.95**
FTO/PCBM/Cs$_2$TiI$_2$Br$_4$/CuSCN/Au *	**10^{13}**	**300**	**7.54**	**8.21**	**1.07**	**85.44**
FTO/PCBM/Cs$_2$TiI$_2$Br$_4$/Spiro-OMeTAD/Au ***	**10^{13}**	**300**	**7.40**	**8.21**	**1.07**	**84.24**

* This work.
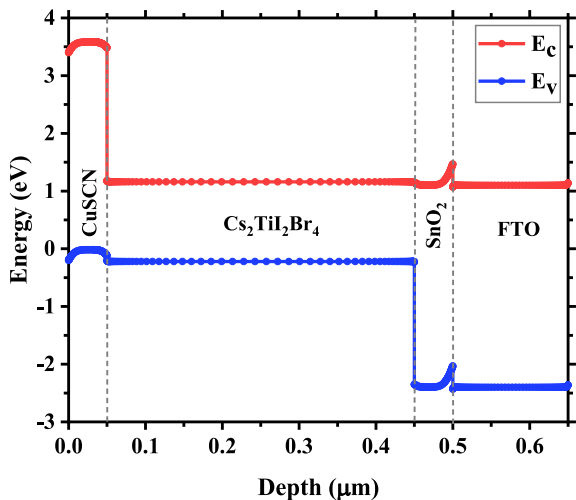
Fig. 9. Simulated band diagram of our proposed device: FTO/SnO$_2$/Cs$_2$TiI$_2$Br$_4$/CuSCN/Au.

CBO plays a pivotal role in interface recombination.

4. Effects of different factors on PSC

This section delt with mainly three factors such as: metal work functions, resistance, and working temperature on the performance of optimized FTO/SnO$_2$/Cs$_2$TiI$_2$Br$_4$/CuSCN/Au perovskite solar cell. From the observation we can compare how this PSC works with varying the metal work-function (φ), series resistance (R$_s$) and shunt resistance (R$_{sh}$), and finally working temperature. All the computational procedures and behavioral findings are discussed thoroughly in the next three sub-sections.

4.1. Effects of metal work-function

To select the best back contact for PSC applications utilizing Cs$_2$TiI$_2$Br$_4$, we evaluated the optimized PSC with different types of materials and various metal work functions. The materials we used consisted of copper (Cu), silver (Ag), iron (Fe), niobium (Nb), carbon (C), and gold (Au). A comparison of the overall performance of various back contacts utilized for the PSC is given in Table 4. Because of the higher V$_{OC}$ and greater ohmic nature of the contact, the majority of barrier height drops in materials with higher work functions.

From Table 4 and Fig. 10 (a) and we can see that the metals having work functions of 4.9 eV, 5.0 eV, and 5.1 eV have somewhat similar performance cell efficiency for the SnO$_2$/Cs$_2$TiI$_2$Br$_4$/CuSCN-based device and performance variation can be noticed for work-function below 4.9 eV.

Our optimized device consists of CuSCN as HTL. CuSCN with Au (gold) back contact can cause device decomposition. So, alternate back contact is an important factor. We can come to the conclusion that the efficiency of our device remains almost the same as before if we use carbon as back contact. The problem of metal and halogens interacting with the electrodes was solved by using carbon or conducting metal oxides as electrodes. This allowed the perovskite cells to work for over 1000 h under sunlight or at temperatures up to 85 °C [51,52]. So, in our Cs$_2$TiI$_2$Br$_4$-based novel PSC, carbon can serve as a prominent and affordable replacement for the gold metal back contact.

4.2. Effects of series and shunt resistance

We have performed a thorough analysis on the influence of series and shunt resistance on the power conversion efficiency (PCE) of the optimized FTO/SnO$_2$/Cs$_2$TiI$_2$Br$_4$/CuSCN/Au device. To isolate the impact of one variable, the other variable was held constant at a

Table 4
Performance comparison of different back contact in FTO/SnO$_2$/Cs$_2$TiI$_2$Br$_4$/CuSCN/Au.

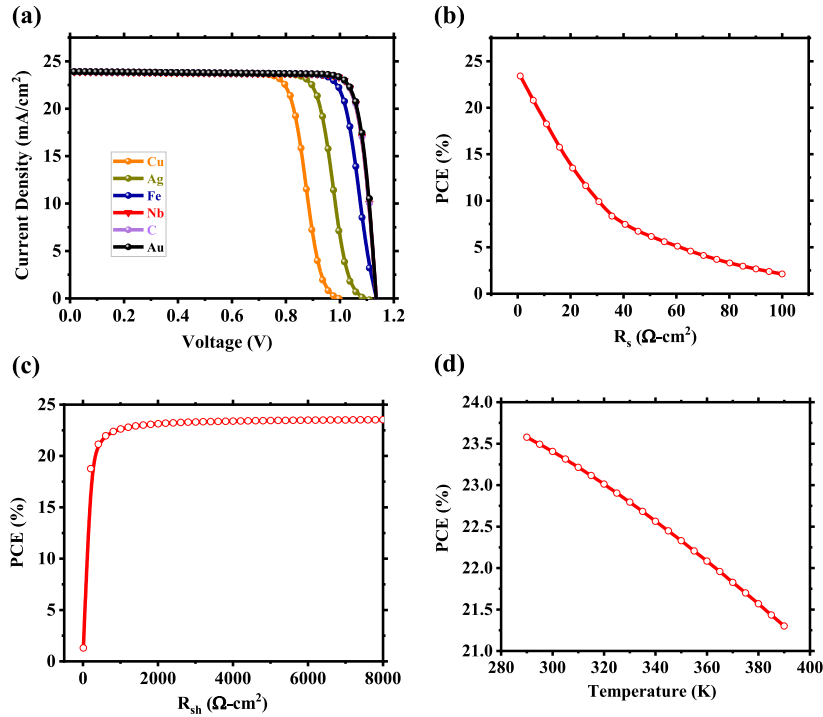| Metal	Cu	Ag	Fe	Nb	C	Au
Work-function (φ)	4.6	4.7	4.8	4.9	5.0	5.1
PCE (%)	18.03	20.30	22.45	23.35	23.40	23.41
V$_{OC}$ (V)	1.02	1.11	1.14	1.14	1.14	1.14
J$_{SC}$ (mA/cm^2)	23.897	23.898	23.899	23.900	23.901	23.901
FF (%)	74.02	76.78	82.76	86.02	86.194	86.197

Fig. 10. Effects of (a) metal work functions; (b) series resistance; (c) shunt resistance; and (d) working temperature on FTO/SnO$_2$/Cs$_2$TiI$_2$Br$_4$/CuSCN/Au structure.

value that yielded optimal performance. As a result, we set the shunt resistance to 4200 Ω-cm^2 to examine the influence of the series resistance and set the series resistance to 1 Ω-cm^2 to examine the influence of the shunt resistance. Series resistance hinders current flow in a solar cell. It comes from the cell's internal resistance and electrical contact. A higher series resistance reduces current and lowers the cell's efficiency. On the other hand, shunt resistance is a parallel resistance in the cell. It comes from leakage currents across the junction and materials. Higher shunt resistance reduces current loss and increases power production. This improves the cell's efficiency. To observe the influence of series resistance, R$_s$ we have varied the R$_s$ from 1 Ω-cm^2 to 100 Ω-cm^2 and Fig. 10 (b) indicates the substantial degradation of the device efficiency as R$_s$ increases and thus highlighting the importance of keeping R$_s$ as small as possible for optimum performance. As for the observation of influence of shunt resistance, R$_{sh}$ illustrated in Fig. 10 (c), we can see a sharp increase of device efficiency till 10^3 Ω-cm^2 and after that the efficiency starts to saturate with further increase in R$_{sh}$. Overall, anything above 2 × 10^3 Ω-cm^2 can be considered as an ideal R$_{sh}$ value for FTO/SnO$_2$/Cs$_2$TiI$_2$Br$_4$/CuSCN/Au device.

4.3. Effects of working temperature

Understanding the devices' behavior in the environment, in this section we are analyzing working temperature in between 290 K and 390 K. There lies some significance in observing the effects of working temperature, as the increase of temperature, the saturation current and the recombination of electron-hole pairs increases. Other positive effects impacted by increasing temperature is that production of thermal charge carriers and also the reduction of bandgap. Fig. 10 (d) illustrates the PCE evaluation of FTO/SnO$_2$/Cs$_2$TiI$_2$Br$_4$/CuSCN/Au structure. The PCE of the device decreases with corresponding increase in the temperature.

5. Conclusion

We conducted a comprehensive investigation with a promising halide double perovskite material, Cs$_2$TiI$_2$Br$_4$, as the absorber layer of a single-junction perovskite solar cell. We theoretically studied both organic and inorganic transport materials and analyzed their performance. In this intensive numerical investigation, we worked with 14 different carrier transport materials to figure out the best carrier transport materials (hole/electron) that provide the best performance, along with their compatibility with Cs$_2$TiI$_2$Br$_4$-based PSCs. Our study led us to a combination of all-inorganic carrier transport materials with an overall structure of FTO/SnO$_2$/Cs$_2$TiI$_2$Br$_4$/CuSCN/Au that outperforms other combinations of carrier transport layers with a PCE of 23.41 %, V$_{OC}$ of 1.141 V, J$_{SC}$ of 23.90 mA/cm^2, and FF of 86.20 % for an optimized absorber layer thickness of 400 nm. The device possesses quantum efficiency up to 82 % within the visible spectrum. We also computed a comparison of different back-contacts, effects of shunt and series resistance, and the influence of working temperature for the device. We propose that carbon can be a more stable and low-cost alternative to gold back-

contacts for Cs₂TiI₂Br₄-based PSCs.

CRediT authorship contribution statement

Tasnim Tareq Ferdous: Writing – original draft, Visualization, Software, Investigation, Formal analysis. **Sadia Sultana Urmi:** Visualization, Software. **Md Abdul Kaium Khan:** Writing – review & editing, Supervision, Resources, Project administration, Conceptualization. **Mohammad Abdul Alim:** Supervision.

Declaration of competing interest

We wish to confirm that there are *no known conflicts of interest* associated with this publication.

Data availability

Data will be made available on request.

Acknowledgements

Appendix A. Supplementary data

Supplementary data to this article can be found online at https://doi.org/10.1016/j.micrna.2024.207881.

References

[1] A.S. Bhalla, R. Guo, R. Roy, The perovskite structure—a review of its role in ceramic science and technology, Mater. Res. Innovat. 4 (1) (2000) 3–26, https://doi.org/10.1007/s100190000062.

[2] N.-G. Park, Perovskite solar cells: an emerging photovoltaic technology, Mater. Today 18 (2) (2015) 65–72, https://doi.org/10.1016/j.mattod.2014.07.007.

[3] G. Szabó, N.G. Park, F. De Angelis, P.V. Kamat, Are perovskite solar cells Reaching the efficiency and voltage limits? ACS Energy Lett. 8 (9) (2023) 3829–3831, https://doi.org/10.1021/acsenergylett.3c01649.

[4] M.A. Green, E.D. Dunlop, M. Yoshita, N. Kopidakis, K. Bothe, G. Siefer, X. Hao, Solar Cell Efficiency Tables (Version 62) (No. NREL/JA-5900-86382), National Renewable Energy Laboratory (NREL), Golden, CO (United States), 2023, https://doi.org/10.1002/pip.3726.

[5] M.-G. Ju, M. Chen, Y. Zhou, H.F. Garces, J. Dai, L. Ma, N.P. Padture, X.C. Zeng, Earth-abundant nontoxic titanium (iv)-based vacancy-ordered double perovskite halides with tunable 1.0 to 1.8 ev bandgaps for photovoltaic applications, ACS Energy Lett. 3 (2) (2018) 297–304, https://doi.org/10.1021/acsenergylett.7b01167.

[6] Seok Joo Yang, Haedam Jin, Jeongbeom Cha, Mi Kyong Kim, Dohun Baek, Hyemi Na, Min Kim, Elucidating degradation mechanisms of mixed cation formamidinium-based perovskite solar cells under device operation conditions, Appl. Surf. Sci. 612 (2023) 155805, https://doi.org/10.1016/j.apsusc.2022.155805. ISSN 0169-4332.

[7] J.P. Correa-Baena, M. Saliba, T. Buonassisi, M. Grätzel, A. Abate, W. Tress, A. Hagfeldt, Promises and challenges of perovskite solar cells, Science 358 (6364) (2017) 739–744, https://doi.org/10.1126/science.aam6323.

[8] Xin Meng, Xueying Tian, Shasha Zhang, Jing Zhou, Yiqiang Zhang, Zonghao Liu, Wei Chen, In situ characterization for understanding the degradation in perovskite solar cells, Sol. RRL 6 (7) (2022) 2200280, https://doi.org/10.1002/solr.202200280.

[9] Z. Xiao, Y. Yan, Progress in theoretical study of metal halide perovskite solar cell materials, Adv. Energy Mater. 7 (22) (2017) 1701136, https://doi.org/10.1002/aenm.201701136.

[10] F. Giustino, H.J. Snaith, Toward lead-free perovskite solar cells, ACS Energy Lett. (2016, December 9), https://doi.org/10.1021/acsenergylett.6b00499. American Chemical Society.

[11] W. Ke, M.G. Kanatzidis, Prospects for low-toxicity lead-free perovskite solar cells, Nat. Commun. 10 (1) (2019) 965.

[12] L. Serrano-Lujan, N. Espinosa, T.T. Larsen-Olsen, J. Abad, A. Urbina, F.C. Krebs, Tin-and lead-based perovskite solar cells under scrutiny: an environmental perspective, Adv. Energy Mater. 5 (20) (2015) 1501119, https://doi.org/10.1002/aenm.201501119.

[13] M. Grätzel, The light and shade of perovskite solar cells, Nat. Mater. 13 (2014, May 1) 838–842, https://doi.org/10.1038/nmat4065.

[14] H.J. Snaith, Present status and future prospects of perovskite photovoltaics, Nat. Mater. 17 (2018, May 1) 372–376, https://doi.org/10.1038/s41563-018-0071-z.

[15] M.A. Green, A. Ho-Baillie, H.J. Snaith, The emergence of perovskite solar cells, Nat. Photonics 8 (2014) 506–514, https://doi.org/10.1038/nphoton.2014.134.

[16] E. Greul, M.L. Petrus, A. Binek, P. Docampo, T. Bein, Highly stable, phase pure Cs₂AgBiBr₆ double perovskite thin films for optoelectronic applications, J. Mater. Chem. A 5 (37) (2017) 19972–19981, https://doi.org/10.1039/C7TA06816Fi.

[17] G. Volonakis, A.A. Haghighirad, R.L. Milot, W.H. Sio, M.R. Filip, B. Wenger, M.B. Johnston, L.M. Herz, H.J. Snaith, F. Giustino, Cs₂InAgCl₆: a new lead-free halide double perovskite with direct band gap, J. Phys. Chem. Lett. 8 (4) (2017) 772–778, https://doi.org/10.1021/acs.jpclett.6b02682.

[18] M.-G. Ju, J. Dai, L. Ma, X.C. Zeng, Lead-free mixed tin and Germanium perovskites for photovoltaic application, J. Am. Chem. Soc. 139 (23) (2017) 8038–8043, https://doi.org/10.1021/jacs.7b04219.

[19] M. Chen, M.G. Ju, A.D. Carl, Y. Zong, R.L. Grimm, J. Gu, N.P. Padture, Cesium titanium (IV) bromide thin films based stable lead-free perovskite solar cells, Joule 2 (3) (2018) 558–570, https://doi.org/10.1016/j.joule.2018.01.009.

[20] K. Chakraborty, M.G. Choudhury, S. Paul, Numerical study of Cs₂TiX₆ (X = Br⁻, I⁻, F⁻ and Cl⁻) based perovskite solar cell using SCAPS-1D device simulation, Sol. Energy 194 (2019) 886–892, https://doi.org/10.1016/j.solener.2019.11.005.

[21] M. Samanta, S.I. Ahmed, K.K. Chattopadhyay, C. Bose, Role of various transport layer and electrode materials in enhancing performance of stable environment-friendly Cs₂TiBr₆ solar cell, Optik 217 (2020), https://doi.org/10.1016/j.ijleo.2020.164805.

[22] S. Ahmed, F. Jannat, Md A.K. Khan, M.A. Alim, Numerical development of eco-friendly Cs_2TiBr_6 based perovskite solar cell with all-inorganic charge transport materials via SCAPS-1D, Optik 165765 (2020), https://doi.org/10.1016/j.ijleo.2020.165765.

[23] M.R. Jani, M.T. Islam, S.M. Al Amin, M.S. Us Sami, K.M. Shorowordi, M.I. Hossain, S. Ahmed, Exploring solar cell performance of inorganic Cs_2TiBr_6 halide double perovskite: a numerical study, Superlattice. Microst. 146 (2020), https://doi.org/10.1016/j.spmi.2020.106652.

[24] S. Moiz, A. Alahmadi, Design of dopant and lead-free novel perovskite solar cell for 16.85% efficiency, Polymers 13 (2021) 2110, https://doi.org/10.3390/polym13132110.

[25] S.A. Moiz, A.N.M. Alahmadi, A.J. Aljohani, Design of a novel lead-free perovskite solar cell for 17.83% efficiency, IEEE Access 9 (2021) 54254–54263, https://doi.org/10.1109/ACCESS.2021.3070112.

[26] S.A. Moiz, Optimization of hole and electron transport layer for highly efficient lead-free Cs_2TiBr_6-based perovskite solar cell, Photonics 9 (2022) 23, https://doi.org/10.3390/photonics9010023.

[27] M.A.K. Khan, S.S. Urmi, T.T. Ferdous, S. Azam, M.A. Alim, Highly efficient Cesium Titanium (IV) Bromide perovskite solar cell and its point defect investigation: a computational study, Superlattice. Microst. 156 (2021) 106946, https://doi.org/10.1016/j.spmi.2021.106946.

[28] K. Shivesh, I. Alam, A.K. Kushwaha, M. Kumar, S.V. Singh, Investigating the theoretical performance of Cs_2TiBr_6-based perovskite solar cell with La-doped $BaSnO_3$ and $CuSbS_2$ as the charge transport layers, Int. J. Energy Res. 46 (5) (2022) 6045–6064, https://doi.org/10.1002/er.7546.

[29] O. Ahmad, A. Rashid, M.W. Ahmed, M.F. Nasir, I. Qasim, Performance evaluation of Au/p-CdTe/Cs_2TiI_6/n-TiO_2/ITO solar cell using SCAPS-1D, Opt. Mater. 117 (2021) 111105, https://doi.org/10.1016/j.optmat.2021.111105.

[30] K. Chakraborty, M.G. Choudhury, S. Paul, Study of physical, optical, and electrical properties of cesium titanium (IV)-Based single halide perovskite solar cell, IEEE J. Photovoltaics 11 (2) (2021) 386–390, https://doi.org/10.1109/JPHOTOV.2021.3050268.

[31] P. Zhao, J. Su, Y. Guo, L. Wang, Z. Lin, Y. Hao, X. Ouyang, J. Chang, Cs_2TiI_6: a potential lead-free all-inorganic perovskite material for ultrahigh-performance photovoltaic cells and alpha-particle detection, Nano Res. 15 (3) (2022) 2697–2705, https://doi.org/10.1007/s12274-021-3801-5.

[32] S.S. Urmi, M.A.K. Khan, T.T. Ferdous, D. Adinehloo, V. Perebeinos, M.A. Alim, Cs_2TiI_6 ($Cs_2TiI_xBr_{6-x}$) halide perovskite solar cell and its point defect analysis, Nanomaterials 13 (14) (2023) 2100, https://doi.org/10.3390/nano13142100.

[33] W. Shockley, H. Queisser, Detailed balance limit of efficiency of p–n junction solar cells, in: Renewable Energy, Routledge, 2018. Vol2_35-Vol2_54).

[34] O.D. Miller, E. Yablonovitch, S.R. Kurtz, Strong internal and external luminescence as solar cells approach the Shockley–Queisser limit, IEEE J. Photovoltaics 2 (3) (2012) 303–311.

[35] Hejin Yan, Yingfeng Li, Li Xiang, Bingxin Wang, Meicheng Li, Hot carrier relaxation in $Cs_2TiI_yBr_{6-y}$ (y= 0, 2 and 6) by a time-domain ab initio study, RSC Adv. 10 (2) (2020) 958–964.

[36] D. Liu, W. Zha, R. Yuan, J. Chen, R. Sa, A first-principles study on the optoelectronic properties of mixed-halide double perovskites $Cs_2TiI_{6-x}Br_x$, New J. Chem. 44 (32) (2020) 13613–13618.

[37] M. Burgelman, P. Nollet, S. Degrave, Modelling polycrystalline semiconductor solar cells, Thin Solid Films 361−362 (2000) 527–532.

[38] T. Minemoto, M. Murata, Impact of work function of back contact of perovskite solar cells without hole transport material analyzed by device simulation, Curr. Appl. Phys. 14 (11) (2014) 1428–1433, https://doi.org/10.1016/j.cap.2014.08.002.

[39] M.K. Hossain, M.H.K. Rubel, G.I. Toki, I. Alam, M.F. Rahman, H. Bencherif, Effect of various electron and hole transport layers on the performance of CsPbI3-based perovskite solar cells: a numerical investigation in DFT, SCAPS-1D, and wxAMPS frameworks, ACS Omega 7 (47) (2022) 43210–43230, https://doi.org/10.1021/acsomega.2c05912.

[40] M.K. Hossain, G.I. Toki, A. Kuddus, M.K. Mohammed, R. Pandey, J. Madan, D.P. Samajdar, Optimization of the architecture of lead-free CsSnCl3-perovskite solar cells for enhancement of efficiency: a combination of SCAPS-1D and wxAMPS study, Mater. Chem. Phys. 308 (2023) 128281, https://doi.org/10.1016/j.matchemphys.2023.128281.

[41] M.K. Hossain, M.S. Uddin, G.I. Toki, M.K. Mohammed, R. Pandey, J. Madan, D.K. Dwivedi, Achieving above 24% efficiency with non-toxic CsSnI3 perovskite solar cells by harnessing the potential of the absorber and charge transport layers, RSC Adv. 13 (34) (2023) 23514–23537, https://doi.org/10.1039/D3RA02910G.

[42] M. Shamna, K. Sudheer, Simulation and optimization of CH3NH3SnI3 based inverted perovskite solar cell with NiO as Hole transport material, Mater. Today: Proc. 33 (2020) 1246–1251, https://doi.org/10.1016/j.matpr.2020.03.488.

[43] F. Azri, A. Meftah, N. Sengouga, A. Meftah, Electron and hole transport layers optimization by numerical simulation of a perovskite solar cell, Sol. Energy 181 (2019) 372–378, https://doi.org/10.1016/j.solener.2019.02.017.

[44] Y. Raoui, S. Kazim, Y. Galagan, H. Ez-Zahraouy, S. Ahmad, Harnessing the potential of lead-free Sn–Ge based perovskite solar cells by unlocking the recombination channels, Sustain. Energy Fuels 5 (18) (2021) 4661–4667, https://doi.org/10.1039/D1SE00687H.

[45] M. Kumar, A. Kumar, A. Raj, P.C. Sati, M. Sahni, A. Anshul, Organic-inorganic perovskite-based solar cell designs for high conversion efficiency: a comparative study by SCAPS simulation, Mater. Today: Proc. 49 (2022) 3081–3087, https://doi.org/10.1016/j.matpr.2020.11.035.

[46] Sadanand Naureen, P. Lohia, D.K. Dwivedi, S. Ameen, A comparative study of quantum dot solar cell with two different ETLs of WS2 and IGZO using SCAPS-1D simulator, Solar 2 (3) (2022, August) 341–353, https://doi.org/10.3390/solar2030020. MDPI.

[47] C.C. Boyd, R. Cheacharoen, T. Leijtens, M.D. McGehee, Understanding degradation mechanisms and improving stability of perovskite photovoltaics, Chem. Rev. 119 (5) (2018) 3418–3451, https://doi.org/10.1021/acs.chemrev.8b00336.

[48] T. Leijtens, G.E. Eperon, S. Pathak, A. Abate, M.M. Lee, H.J. Snaith, Overcoming ultraviolet light instability of sensitized TiO_2 with meso-superstructured organometal tri-halide perovskite solar cells, Nat. Commun. 4 (1) (2013) 2885.

[49] F. Bella, G. Griffini, J.P. Correa-Baena, G. Saracco, M. Grätzel, A. Hagfeldt, C. Gerbaldi, Improving efficiency and stability of perovskite solar cells with photocurable fluoropolymers, Science 354 (6309) (2016) 203–206, https://doi.org/10.1126/science.aah4046.

[50] G.K. Grandhi, D. Hardy, M. Krishnaiah, B. Vargas, B. Al-Anesi, M.P. Suryawanshi, P. Vivo, Wide-bandgap perovskite-inspired materials: defect-driven challenges for high-performance optoelectronics, Adv. Funct. Mater. (2023) 2307441.

[51] C.C. Boyd, R. Cheacharoen, K.A. Bush, R. Prasanna, T. Leijtens, M.D. McGehee, Barrier design to prevent metal-induced degradation and improve thermal stability in perovskite solar cells, ACS Energy Lett. 3 (7) (2018) 1772–1778, https://doi.org/10.1021/acsenergylett.8b00092.

[52] K.A. Bush, A.F. Palmstrom, Z.J. Yu, M. Boccard, R. Cheacharoen, J.P. Mailoa, M.D. McGehee, 23.6%-efficient monolithic perovskite/silicon tandem solar cells with improved stability, Nat. Energy 2 (4) (2017) 1–7.

[53] P.K. Kung, M.H. Li, P.Y. Lin, Y.H. Chiang, C.R. Chan, T.F. Guo, P. Chen, A review of inorganic hole transport materials for perovskite solar cells, Adv. Mater. Interfac. 5 (22) (2018) 1800882.

[54] P. Kumar, M. Eriksson, D.S. Kharytonau, S. You, M.M. Natile, A. Vomiero, All-inorganic hydrothermally processed semitransparent Sb_2S_3 solar cells with CuSCN as the hole transport layer, ACS Appl. Energy Mater. 7 (4) (2024) 1421–1432.

[55] M. Jung, Y.C. Kim, N.J. Jeon, W.S. Yang, J. Seo, J.H. Noh, S. Il Seok, Thermal stability of CuSCN hole conductor-based perovskite solar cells, ChemSusChem 9 (18) (2016) 2592–2596.

[56] A. Nizamuddin, F. Arith, J. Rong, M. Zaim, A.S. Rahimi, S. Saat, Investigation of copper (I) thiocyanate (CuSCN) as a hole transporting layer for perovskite solar cells application, J. Adv. Res. Fluid Mech. Thermal Sci. 78 (2) (2021) 153–159.